## Liftoff of a Soft-Actuated Micro-Aerial-Robot Powered by Triboelectric Nanogenerators

Younghoon Lee<sup>a,b</sup>, Zhijian Ren<sup>a</sup>, Yi-Hsuan Hsiao<sup>a</sup>, Suhan Kim<sup>a</sup>, Won Jun Song<sup>c</sup>, Chengkuo Lee<sup>d</sup>, Yufeng Chen<sup>a</sup>\*

<sup>a</sup>Department of Electrical Engineering and Computer Science, Massachusetts Institute of Technology, Cambridge, Massachusetts 02139, United States.

<sup>b</sup>Department of Mechanical Engineering, Gachon University, Seongnam 13120, South Korea.

<sup>c</sup>Department of Material Science and Engineering, Seoul National University, 1 Gwanak-ro, Gwanak-gu, Seoul, 08826, South Korea.

<sup>d</sup>Department of Electrical & Computer Engineering, National University of Singapore, 4 Engineering Drive 3, Singapore, 117576 Singapore.

\*Corresponding author: yufengc@mit.edu

#### **Abstract**

Aerial insects can nimbly navigate in cluttered natural environments while they interact with delicate objects such as flowers and leaves. To achieve insect-like agility and robustness, power dense dielectric elastomer actuators (DEAs) have been developed for driving sub-gram micro-aerial-vehicles (MAVs). However, despite exhibiting muscle-like bandwidth and resilience, DEAs require a high driving voltage in the range of 1 – 2 kilovolts. This requirement poses substantial challenges for developing compact boost electronics and energy sources, which prohibit power autonomous operations of soft-actuated sub-gram MAVs. Here, we develop a compact and high power triboelectric nanogenerator (TENG) that can effectively charge a high-voltage DEA and enable the liftoff of a soft-actuated MAV. We propose an Inplane Charge Pump (ICP) design that can deliver over 1500 V and 110 mW without requiring a secondary charge pump or magnetic circuit components such as inductors or transformers. Compared to conventional free-standing mode TENGs, our ICP design shows a 280% and 920% increase in voltage and energy generation, respectively. When this TENG powers a DEA-driven MAV, the 160 mg robot achieves liftoff while carrying a 144 mg payload. This result highlights the potential of powering high-voltage microrobots with energy-harvesting devices.

# **Graphical Abstract**



This work presents a compact triboelectric nanogenerator (TENG) for powering an insect-scale microaerial-vehicle (MAV). The TENG employs an in-plane charge pump design and generates over 1500 V and 110 mW. It drives a 160 mg flapping-wing MAV at 400 Hz and enables robot liftoff. This result highlights the potential of driving high voltage soft artificial muscles with energy harvesting devices.

**Keywords:** dielectric elastomer actuator, triboelectric nanogenerators, soft robotics, flapping-wing, microaerial-vehicles

## 1. Introduction

Owing to their small size and diminishing inertia, insect-scale micro-aerial-vehicles (MAVs) have the potential to explore and inspect cluttered and unstructured environments that are challenging for larger scale drones. At the millimeter scale, electric motors become unfavorable due to adverse torque density scaling. This shortcoming inspires the development of miniature actuators such as piezoelectric ceramics[1] and electrohydrodynamic thrusters[2]. These actuators led to hovering flights in sub-gram MAVs[3], and they further enabled insect-like flight demonstrations such as perching[4] and multimodal locomotion[5]. However, unlike insects that can fly in a swarm and robustly interact with the surrounding environment, most MAVs are limited to operating in open spaces because they are fragile against collisions. This shortcoming limits the application of existing microscale robots.

To address this challenge, soft artificial muscles[6] have been developed for improving the resilience of microrobotic systems[7]. Among existing soft actuators, dielectric elastomer actuators (DEAs)[6] exhibit high power density and resemble muscle-like robustness. Our prior works[8] demonstrated DEA-driven aerial robots can recover from in-flight collisions, endure severe damage, and perform agile acrobatic maneuvers. These unique flight capabilities highlight the advantages of DEAs over rigid microscale actuators. However, DEAs require a high actuation voltage (500 – 5000 V), which poses substantial challenges on incorporating onboard energy sources and boost electronics. Given the severely constrained payload in sub-gram MAVs, there exist two bottlenecks in designing onboard boost electronics. First, boost circuits require heavy (>100 mg) magnetic components such as inductors and transformers, and they are inefficient when switched at high frequencies (>100 kHz). Second, there is a lack of lightweight (<20 mg) and high voltage (>1 kV) switches for controlling the boost circuit. Consequently, existing sub-gram boost circuits[9, 10] for DEAs only achieved 600 V with less than 10% efficiency. These limitations motivate the need to explore alternative power sources that do not require batteries and heavy boost electronics.

In contrast to batteries and fuel cells that store and release energy, energy harvesters convert ambient solar, thermal, and mechanical energy into electricity. While most energy harvesters cannot generate high voltages as required by DEAs, triboelectric nanogenerators (TENGs)[11-13] have shown high voltage generation of up to 20 kV[14-16] without requiring heavy boost electronics. This high voltage generation has enabled a suite of self-powered sensors[17-20], actuators[21, 22], and medical device demonstrations[23, 24]. However, DEAs require high power to drive robotic systems, posing substantial challenges for most TENGs that only supply micro-amps of current.[25] There are three recent TENG developments aimed at improving output power: surface modification, instantaneous discharge, and secondary charge pump.[26] Surface modification involves creating micro/nano morphology and applying chemical coatings on the TENG to augment contact electrification, but it is susceptible to surface wear

when the device operates at a high contacting speed[27, 28]. Instantaneous discharge increases the peak output power through quickly switching an external control circuit, but it does not improve average power and its efficiency reduces under a high impedance load[29, 30]. Charge pumping is a design that consists of a main TENG and a pump TENG[16, 31]. While the main TENG stores charge, a secondary pump TENG injects additional charge to increase output power. While this design is effective, it requires a secondary pump, which can be difficult to incorporate on a mobile robot.[32] To address the abovementioned challenges, we need a high voltage, high power, durable, and compact energy harvester for powering DEA-driven mobile robots.

We propose a new approach for driving high voltage microscale robots. We envision future robots will operate in a team where larger terrestrial robots will support intermittent flights of MAVs (Fig. 1a). Compared to MAVs, terrestrial robots can easily carry onboard batteries, sensors, and control electronics due to having lower cost-of-transport and higher payload. Fig. 1a illustrates an autonomous terrestrial robot that traverses natural environments while carrying two DEA-driven MAVs. The robot's foot pads are equipped with TENGs for harvesting mechanical energy. When the robot reaches an object of interest such as a flower, the MAVs can take off from the terrestrial robot using the harvested energy. This energy harvesting and storage system can deliver high-voltage driving signals without requiring heavy magnetic components, which offers an alternative for DEA-driven MAVs.

Here, we develop a compact and durable TENG for powering high-voltage and high-power MAVs. We propose an In-plane Charge Pump (ICP) design (Fig. 1b) that substantially increases the TENG output voltage and power without requiring a separately located charge pump. Compared to traditional free-standing mode TENGs, our new generator can produce 280% higher voltage and 920% higher energy. When this TENG is connected to a voltage doubler and energy storage circuit, it can power a DEA-driven flapping-wing aerial robot (Fig. 1c). This 160 mg biomimetic MAV operates at 1540 V and 400 Hz (Fig.

1d), and it can lift a 144 mg payload during takeoff. This result represents the first MAV liftoff demonstration (Fig. 1e) enabled by a TENG, which highlights the advantage of high-voltage energy harvesters without requiring batteries and boost electronics.

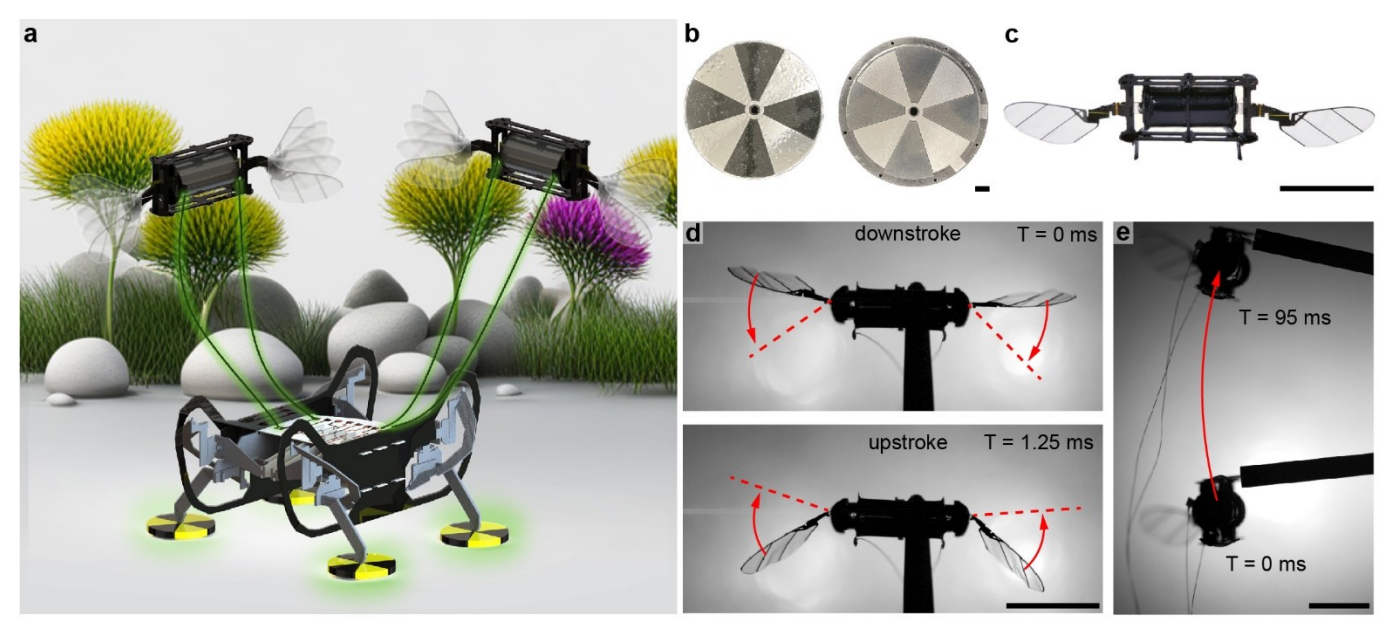


**Fig. 1.** High voltage aerial robots powered by TENGs. a) A conceptual illustration where a larger terrestrial robot collects energy from ambient environments and converts it into electrical energy for driving high-voltage DEAs in aerial robots. b) Rotor and stator of the ICP-TENG. c) A 160 mg DEA-driven micro-aerial-robot. d) Robot flapping-wing motion and e) liftoff demonstration when it is powered by the ICP-TENG. The scale bars in b-e) represent 1 cm.

### 2. Results and discussion

### 2.1. Design of an ICP-TENG

To achieve TENG-powered flight in a soft-actuated robot, the generator needs to deliver high voltage and power while maintaining a compact size. There are numerous prior studies[16, 27, 30] that proposed TENG designs for enhancing output voltage and power. In particular, the use of a secondary charge pump can inject charges into an additional floating conductive layer in the main TENG[16, 33], which increases the output voltage. In addition, a rotary charge TENG design was proposed[31] to improve output power compared to contact separation mode TENGs. However, in these prior works, the secondary charge pump was separated

from the main TENG, requiring extra structure and space that would be difficult to incorporate on a mobile robotic system.

To improve TENG compactness, we propose an ICP-TENG design where the main TENG and the secondary charge pump are placed on the same plane (Fig. 2a). In a side view illustration, Fig. 2a labels the electrodes (grey), the main pump (blue), and the secondary charge pump (orange and yellow). In comparison, the charge pump regions are left as empty space in conventional designs. Fig. 2b illustrates the working principle of our design. First, as the rotor slides along the stator, contact electrification occurs between the rotor electrode (dark grey) and the stator's main TENG (blue). The pumping TENGs (orange and yellow) also become charged (Fig. 2b i). Next, as the rotation continues, the rotor's charge pump region (orange) overlaps with the stator's main TENG (blue). The negatively charged rotor pump (orange) induces an electric field, which pushes the negative charges in the stator's electrode (light grey) into the rotor's electrode (dark grey). Consequently, the combined effects of field induced charge transfer and contact electrification causes a current to flow through the load resistor (Fig. 2b ii). As the rotation continues, the current reverses its direction (Fig. 2b iii-iv), leading to an alternating current through the load.

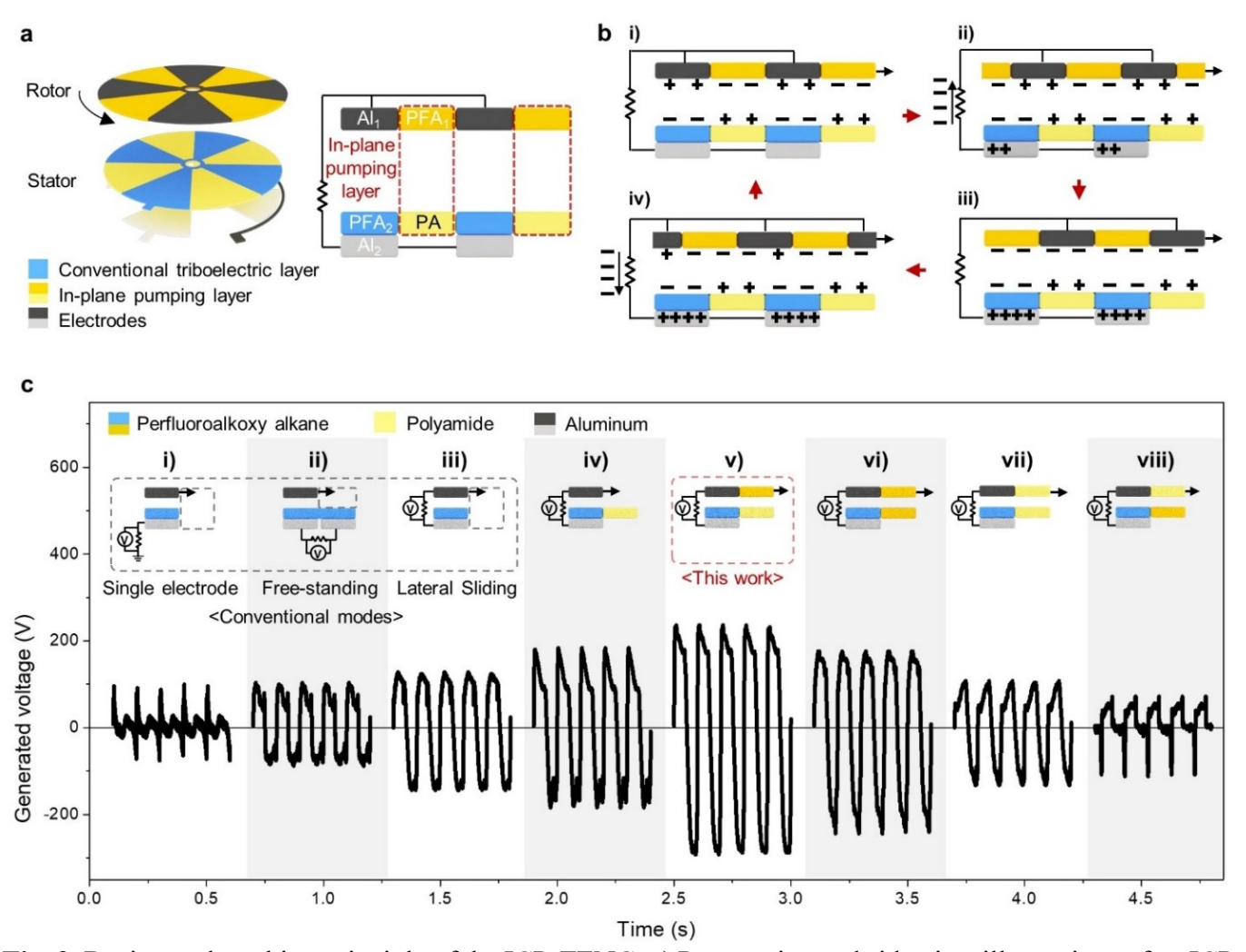


**Fig. 2.** Design and working principle of the ICP-TENG. a) Perspective and side view illustrations of an ICP-TENG where the primary TENG and charge pumps are placed in the same planes. b) Working principle of the ICP-TENG. c) Output voltage comparison between different TENGs of the same size and operating conditions.

To evaluate the effectiveness of this design, we built eight different sliding mode TENGs and compared their performance. Fig. 2c i-iii) show three conventional sliding mode TENGs without charge pumps, and Fig. 2c iv-viii) illustrate five ICP-TENGs with in-plane charge pumps. All these TENGs have the same diameter of 8 cm (Fig. S1, Supplementary Material) and they are driven at the same rotational speed of 10 revolutions per second (rps). Fig. 2c also compares the measured voltage across a 40 M $\Omega$  load for each design. Compared to the free-standing mode design[34] (Fig. 2c ii), our best-performing ICP-TENG (Fig. 2c v) generates 280% higher peak-to-peak voltage ( $V_{pp}$ ) and 920% higher energy. The detailed

measurements are shown in Fig. S1c,d (Supplementary Material). This substantial voltage and energy improvement is critical for powering DEA-driven aerial robots. In the following sections, we describe TENG material selection, design of rectifying circuits, and experiments with DEAs.

## 2.2. Material selection and characterization of ICP-TENG

Based on the proposed ICP-TENG design, we experimented with different stator and rotor materials to maximize the output voltage. **Fig. 3**a and Fig. S2 (Supplementary Material) illustrate the TENG structure where it consists of a central rotor sandwiched by top and bottom stators. We chose perfluoroalkoxy alkane (PFA) as the main TENG material (blue colored region in Fig. 3a) and experimented with different charge pump materials (yellow and orange colored regions in Fig. 3a), which include polyamide (PA), polyethylene terephthalate (PET), polyether ether ketone (PEEK), polyimide (PI), polytetrafluoroethylene (PTFE), fluorinated ethylene propylene (FEP), and PFA.

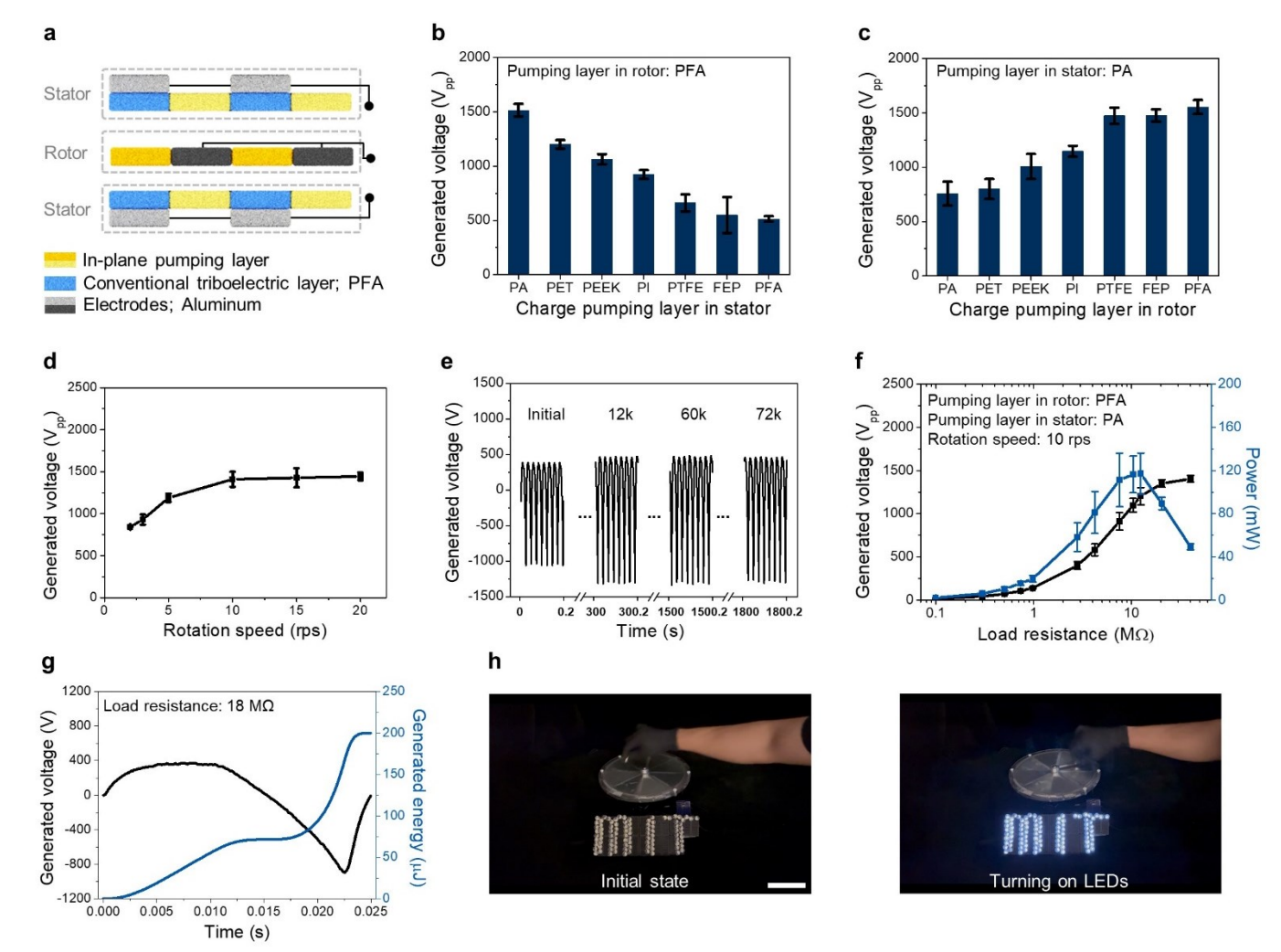


**Fig. 3.** Characterization of an ICP-TENG. a) Our ICP-TENG consists of two stators and one central rotor to increase net output power. The output voltage changes under different charge pump materials in b) the stator and c) the rotor. d) ICP-TENG output voltage as a function of rotation speed. e) The output voltage remains constant during the 1800 s of continuous operation, equivalent to making 72000 contacts. f) Peak output voltage and power under different resistive loads. The output power is maximized at 117.2 mW for an 18 MΩ load. g) Instantaneous output voltage and delivered energy for an 18 MΩ load. h) The ICP-TENG can power 93 series-connected white LEDs that have a turn-on voltage of 3.0 V. The scale bar represents 10 cm.

First, we used PFA to construct the rotor charge pump and vary the stator charge pump materials. The generated voltage varies from 513  $V_{pp}$  to 1513  $V_{pp}$  as the stator material changes from PFA to PA (Fig. 3b). We also varied the rotor materials where the stator charge pump was made of PA. The generated voltage varies from 757  $V_{pp}$  to 1513  $V_{pp}$  for different rotor materials (Fig. 3c). These experiments show that the output voltage is maximized when the charge pump materials have the largest difference of electron

affinities as indicated in the triboelectric series table. This is because a higher difference in electron affinity increases the surface charge density during contact electrification, further leading to a higher output voltage. These experiments also highlight that incorporating an in-plane charge pump substantially improves the TENG performance. Based on these results, we chose PFA and PA as the rotor and stator materials, respectively.

We also characterized the ICP-TENG performance under different operating conditions. The rate of charge accumulation and induction increases as the device rotates at a faster speed. This leads to an increase of measured voltage across a resistive load. As the driving rotation speed increases from 2 to 20 rps, the measured output voltage increases from 842 to 1440  $V_{pp}$  (Fig. 3d). The associated time varying data is reported in Fig. S3 (Supplementary Material). We observed the output voltage plateaus at approximately  $1400 \, V_{pp}$  after the rotational speed exceeds  $10 \, \text{rps}$ , and we decided to conduct the following characterization experiments at  $10 \, \text{rps}$ .

The ICP-TENG demonstrates good endurance against surface wear. Fig. 3e shows the ICP-TENG's output voltage remains constant during 1800 seconds of continuous operation. In addition, we characterized the device's net output voltage and power as a function of load resistance. As we increase a resistive load from 0.1 M $\Omega$  to 40 M $\Omega$ , the output voltage increases from 14 V to 1405 V (Fig. 3f). The peak and average power reach a maximum when the load resistance is 18 M $\Omega$ , and their values are 117 mW and 8 mW, respectively. Fig. 3g further shows the instantaneous output voltage and energy corresponding to a quarter rotation. The output voltage and power represent a substantial improvement compared to conventional TENGs, making it promising for powering high-voltage robotic actuation. To highlight the ICP-TENG performance, we drove 93 white LEDs that were connected in series (Fig. 3h and Video S1, Supplementary Material). Each white LED has a turn-on voltage of 3.0 V, and the LED array is lit by the generator at a gentle rotation speed

of 0.7 rps. This result confirms our ICP-TENG can generate a high driving voltage. In the following section, we will describe DEA actuation based on this ICP-TENG.

### 2.3. High voltage DEA operation powered by an ICP-TENG

We demonstrated the ICP-TENG can power DEAs in a soft-actuated MAV (Fig. 1c). A DEA can be modelled as a soft capacitor where a dielectric elastomer layer is sandwiched by compliant electrode layers. When the electrode layers are charged, electrostatic stress causes the elastomeric layer to compress in its normal direction. Since the elastomer is incompressible, the elastomer layer elongates along its tangential direction, performing mechanical work. Our DEA consists of 7 elastomer layers and 6 interdigitated electrode layers, and this multilayered structure is rolled into a cylindrical shell (**Fig. 4**a).

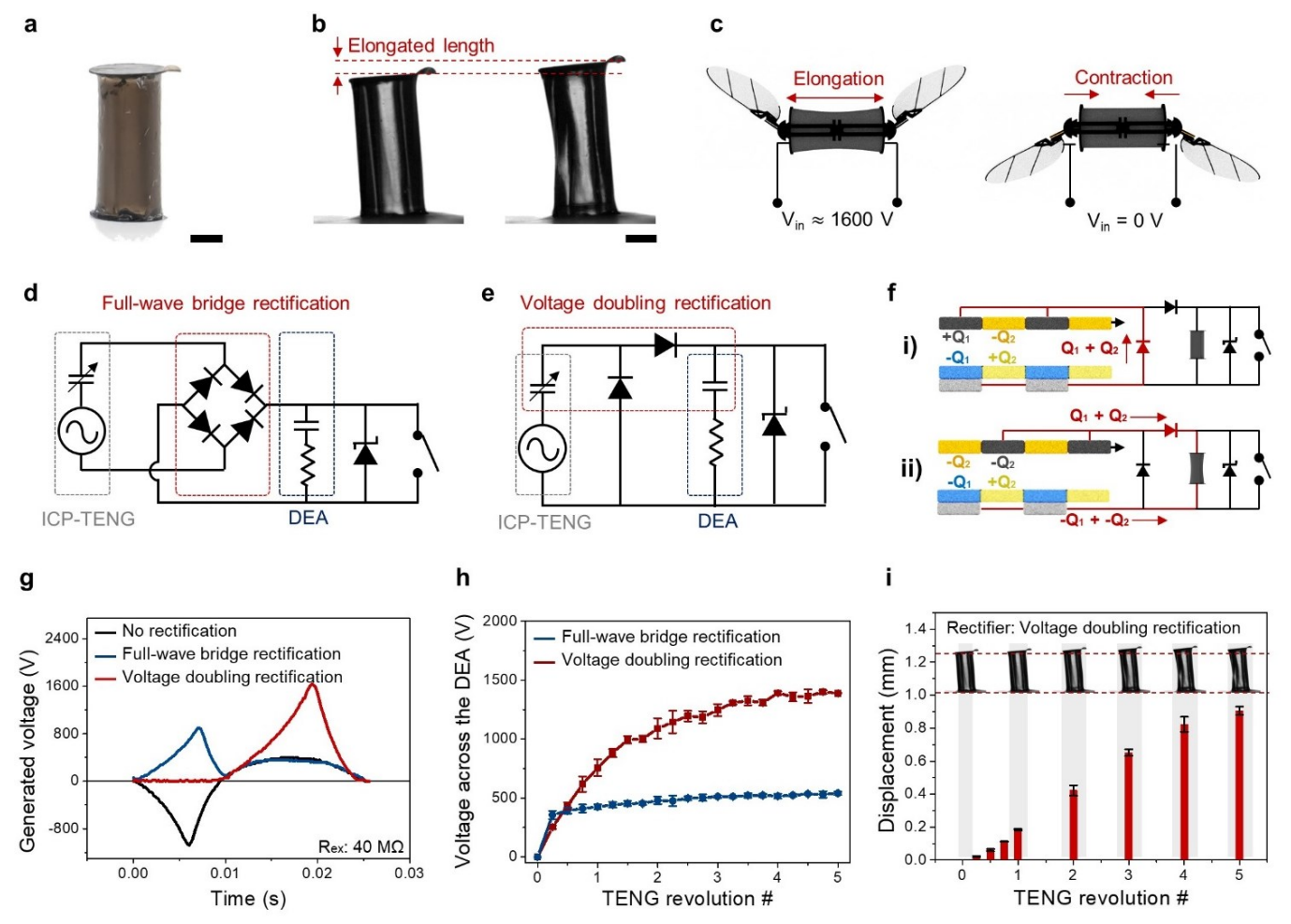


**Fig. 4.** DEAs powered by an ICP-TENG. a) An image of a 100 mg DEA. b) The DEA experiences 13% strain under a 1500 V driving input. c) Schematics that illustrate the robot's flapping-wing motion. Through

linear four-bar transmissions, the DEA's linear actuation drives the robot's wing stroke motion. The ICP-TENG is connected to a DEA via either d) a full-wave rectifier or e) a voltage doubler. f) Working principle of the ICP-TENG when it is connected to a voltage doubler circuit. g) Comparison of output voltage across a 40 M $\Omega$  load when the ICP-TENG is connected to different rectifying circuits. h) Comparison of output voltage across a DEA. The voltage doubler circuit shows 2.8 times higher voltage compared to the full-wave bridge circuit. i) Measured DEA elongation as a function of TENG rotation. Scale bars in a,b) represent 2 mm.

In our prior work, the DEA was driven by a unipolar sinusoidal signal from a high voltage amplifier. When 1500 V is applied on the DEA, it elongates by 13% (Fig. 4b). When the applied voltage reduces to 0 V, the DEA retracts to its original length. The DEA is connected to the robot transmissions and wings, which translate the linear actuation into the robot flapping-wing motion (Fig. 4c). The DEA can be modeled electrically as a series resistor-capacitor (RC) element, which accounts for a DEA's charge storage (C) and electrode resistive loss (R). In this work, the equivalent R and C are 22.1 k $\Omega$  and 1.83 nF, respectively. To drive a DEA, the ICP-TENG needs to charge the equivalent capacitor to 1500 V, which represents 2 mJ of energy  $(\frac{1}{2}CV^2)$  every actuation cycle.

While the ICP-TENG generates bipolar output voltage, a DEA requires unipolar driving signals. We constructed rectifying circuits between the ICP-TENG and the DEA (Fig. 4d,e). In these circuit schematics, the ICP-TENG is modelled as a voltage source and a variable capacitor connected in series, the DEA is modelled as a series capacitor-resistor load, and high voltage Zener diodes are placed in parallel with the DEA for over-voltage protection. The full-wave rectifier (Fig. 4d) converts a bipolar signal into a unipolar signal through using four diodes.

In comparison, the voltage doubler (Fig. 4e) enhances the ICP-TENG output voltage through using only two diodes, leading to smaller conduction and switching losses. Fig. 4f illustrates the working principle of the voltage doubler design. When the ICP-TENG generates negative voltage (Fig. 4f-i), the charges flow to the top electrode through a diode connected in parallel. In this phase, there is no charge delivered to the

DEA. Next, the ICP-TENG generates positive voltage (Fig. 4f-ii) and all stored charges are delivered to the DEA, leading to an enhanced output voltage. Fig. 4g compares ICP-TENG performance when it has no rectification (NR), a full-bridge rectifier (FB), or a voltage doubler (VD). The measurements confirmed that the ICP-TENG without rectification generates bipolar voltage, and the full-wave rectifier and voltage doubler convert the output into positive driving signals. The maximum positive output voltage of the NR, FB, and VD circuits are 400 V, 900 V, and 1640 V, and the corresponding delivered energy to a 40 MΩ load resistor are 104 μJ, 85.4 μJ, and 256.6 μJ (Fig. S4a, Supplementary Material). Compared to the NR case, the FB design shows an 18% energy reduction, which could be contributed from diode conduction and switching losses. In contrast, the VD design shows a 2.5 times increase of delivered energy, which could be contributed by the charge accumulation on the stator shown in Fig. 4f-i. This process further enhances voltage generation when charges flow to the DEA in Fig. 4f-ii. These output voltage and energy improvements are crucial for an ICP-TENG to drive high-voltage DEAs.

We compared the FB and VD performance when they power DEAs. Based on the circuit schematics shown in Fig. 4d-e, we measured the voltage across a DEA as a function of ICP-TENG revolution (Fig. 4h). The ICP-TENG has 4 segments and an angular speed of 10 rps. After completing 5 revolutions, the FB and VD circuits charge the DEAs to 500 V and 1400 V, respectively. The corresponding delivered energy are 270 µJ and 1790 µJ (Fig. S4b, Supplementary Material), showing the VD design is substantially more advantageous. We also measured the DEA elongation as a function of ICP-TENG revolution (Fig. 4i). The DEA has a length of 8 mm, and its elongation reaches 0.9 mm after the ICP-TENG completes 5 rotations (Fig. 4i). This result shows the DEA achieves a static strain of 11.3%.

Since the DEA can be charged to 1400 V after 5 revolutions and the ICP-TENG operates at 10 rps, it implies the ICP-TENG can charge the DEA twice every second. This is sufficient for enabling low frequency robotic actuation, but it cannot demonstrate robot liftoff that requires 400 Hz. To achieve robot liftoff, the drive

circuit must store the energy harvested from an ICP-TENG and release it in a shorter duration. The next section will describe energy storage and control electronics designs that enable aerial robot liftoff.

## 2.4. Soft robot liftoff enabled by an ICP-TENG

We designed a circuit that stores the harvested energy and controls robot operation. This circuit consists of a storage stage and a regulator stage (**Fig. 5**a). First, the storage stage rectifies the TENG-generated voltage and stores the energy in a capacitor  $C_1$ . After  $C_1$  is charged to approximately 1500 V, the regulator stage sends a 400 Hz square wave driving signal to the robot. The regulator stage contains a microcontroller unit (MCU) that controls two switching MOSFETs. In phase 1, the MCU turns on  $Q_1$  and  $Q_2$ , which causes the energy to flow from the storage capacitor  $C_1$  to the DEA (Fig. 5b-i). The high resistance  $R_1$  ensures negligible current dissipates through  $Q_2$ , and most energy flows to  $C_1$ . The DEA charges to a high voltage  $V_H$  and elongates due to electrostatic stress. In phase 2, the MCU turns off  $Q_1$  and  $Q_2$ , which causes the energy to flow from the DEA to a dissipation resistor  $R_2$  (Fig. 5b-ii). The DEA discharges to 0 V and retracts to the minimum length. Phases 1 and 2 alternate at 400 Hz and the resultant driving signal  $V_{DEA}$  resembles a square wave (Fig. 5c).

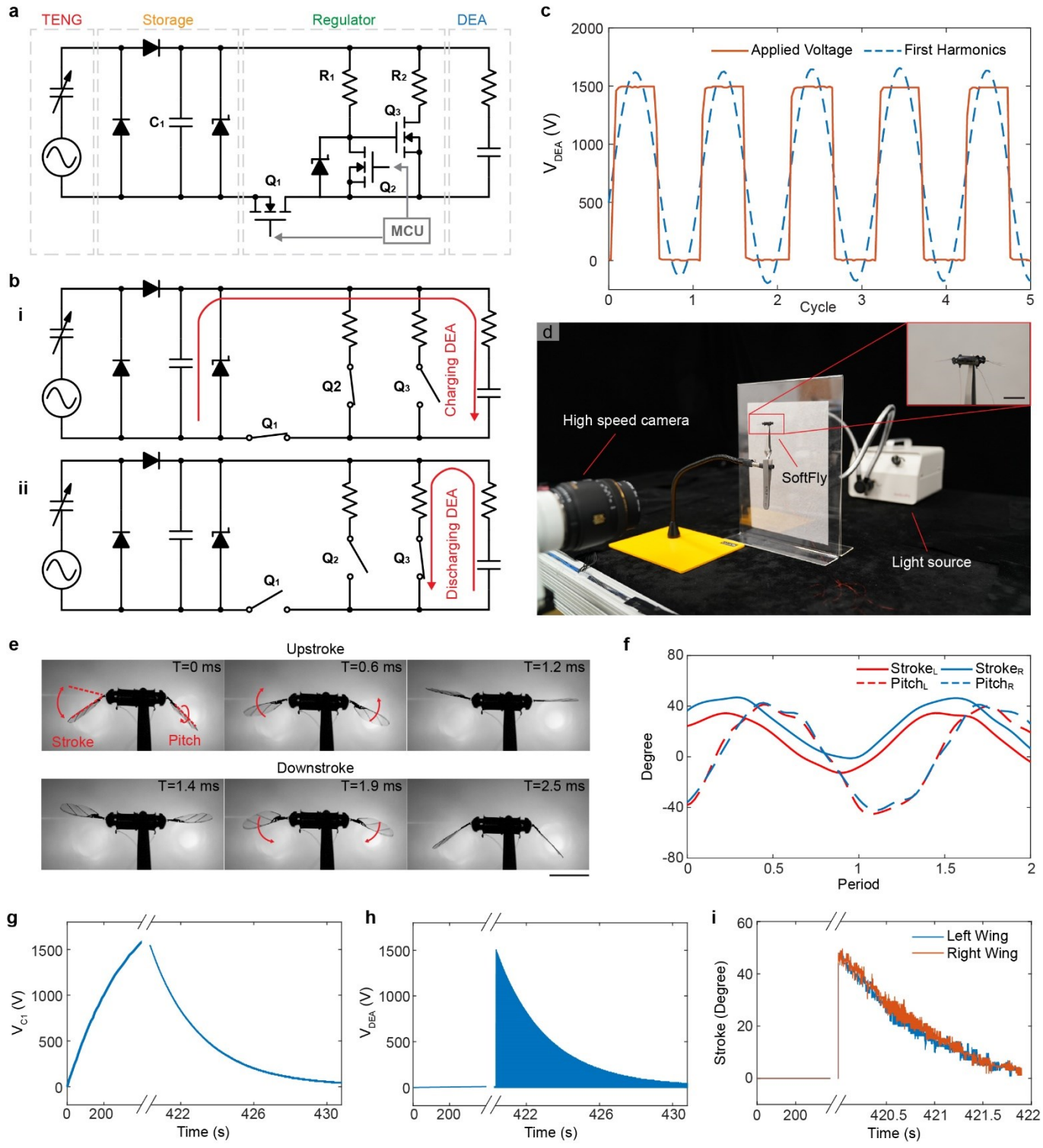


**Fig. 5.** High voltage and high frequency robot operation powered by an ICP-TENG. a) A circuit schematic that consists of the ICP-TENG, energy storage, regulation, and the robot. b) Working principles of the circuit regulator. In each actuation period, the DEA is charged by the storage capacitor and then it discharges through the load resistor. c) The measured driving voltage (orange) across a DEA resembles a square wave. Its fundamental harmonic (blue) has a higher amplitude. d) An image of the static flapping-wing experiment setup. e) An image sequence of the robot flapping-wing motion in one period. f) Tracked

wing stroke and pitch kinematics that correspond to the experiment in e). Measured voltage across g) the storage capacitor and h) the DEA as functions of time. i) Measured wing stroke amplitude as a function of time. Scale bars in d,e) are 1 cm.

In prior MAV works[1, 3-6, 8], most microscale actuators were driven by sinusoidal waveforms. These driving signals minimize the actuation strain rate and prevent rigid actuators (e.g., piezoelectric ceramics) from fracturing. However, it is difficult to generate sinusoidal driving waveforms because they require magnetic components such as inductors and transformers. Our circuit generates a waveform that resembles a square wave (Fig. 5c), which is suitable for driving mechanically robust soft actuators such as a DEA. At the DEA's resonance frequency, the actuation strain is sinusoidal because higher harmonics are filtered by viscoelastic damping. The DEA's response to a square wave is identical to its response to the lowpass filtered harmonic components of the same signal (dashed line in Fig. 5c). In comparison, it is advantageous to drive a DEA with a square wave because it generates similar motion at a lower maximum voltage.

To evaluate the ICP-TENG performance, we conducted static flapping-wing experiments (Fig. 5d). A 160 mg robot was connected to the circuit's output terminal while it is mounted in front of a high-speed camera (Phantom VEO 710). First, the ICP-TENG charged the storage capacitor C<sub>1</sub> to 1500 V. Then the regulator circuit sent a 400 Hz and 1500 V driving signal to the robot. The robot flapped its wings at 400 Hz, and the motion was recorded at 22000 frames per second. Fig. 5e and Video S2 (Supplementary Material) illustrate the wing upstroke and downstroke motion. Based on this high-speed video, we extracted the instantaneous wing stroke and pitch kinematics (Fig. 5f). The measured wing stroke and pitch amplitude are 48° and 80°, respectively. Based on previous aerodynamic models[35], this flapping-wing kinematics correspond to sufficient forces for enabling liftoff.

Fig. 5g-i illustrates the charging and discharging processes during this experiment. The ICP-TENG charged a  $4.5~\mu F$  storage capacitor to 1540~V in 420~seconds – equivalent to generating 5.4~J of energy. During the discharge phase, the electrical energy was sent to the DEA at 400~Hz. In each of the initial flapping-wing

periods, 2.5 mJ of energy flowed to the DEA, and then it was dissipated by the resistor  $R_2$ . During this flapping experiment, the stored energy gradually reduced in the storage capacitor. This caused the capacitor voltage  $V_{C1}$  and the DEA voltage  $V_{DEA}$  to reduce (Fig. 5h). Consequently, the robot stroke motion (Fig. 5i) and the corresponding lift force also reduced as the stored energy decreased.

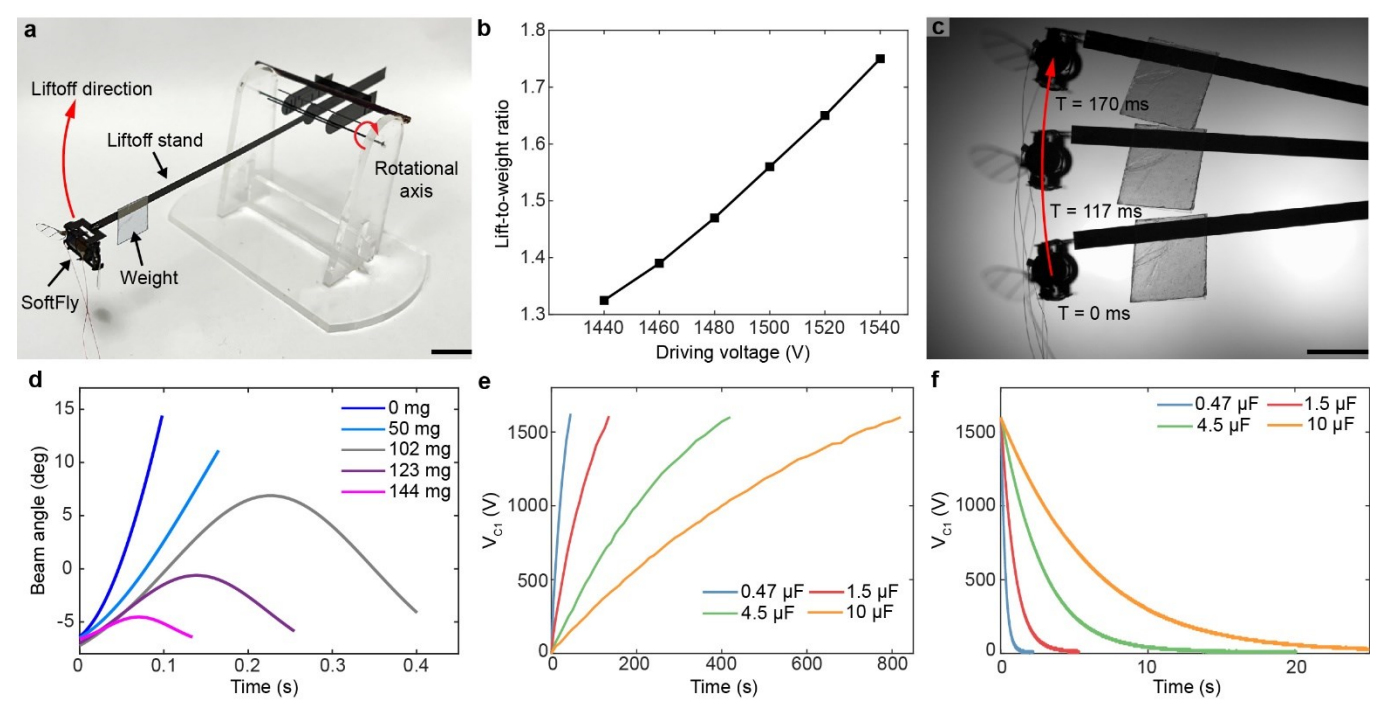


**Fig. 6.** Micro-aerial-robot liftoff demonstration enabled by an ICP-TENG. a) An image of the liftoff experimental setup. b) Measured lift-to-weight ratio as a function of driving voltage. c) A composite image showing robot liftoff while it carries a 50 mg payload. d) Measured beam angle during robot liftoff experiments. Measured voltage amplitude of the storage capacitor during the e) charging and f) discharging phases. The scale bars in a,c) represent 1 cm.

In addition to static-flapping experiments, we also demonstrated robot liftoff. We mounted the robot on a liftoff stand that was balanced around a pivot axis (**Fig. 6**a). If the robot generates a lift force that exceeds its weight, then it ascends upward. Fig. 1e and Video S3 (Supplementary Material) show a composite image of robot liftoff. Without carrying payload, the robot ascended by 2.7 cm in 95 ms. We measured the lift force by tracking the rotation angle and then fitting the motion to a dynamic model[8]. We varied the initial voltage from 1440 to 1540 V, and we found the robot's lift-to-weight ratio increased from 1.32 to 1.75 (Fig. 6b).

We also conducted payload lifting experiments where an added mass was mounted on the balance beam. The robot ascends 2.6 cm in 150 ms while it carries a 50 mg payload (Fig. 6c). We repeated the experiments while the robot carries payloads of 102 mg, 123 mg, and 144 mg. These liftoff experiments are shown in Fig. S5 (Supplementary Material) and Video S4 (Supplementary Material), and the corresponding beam angle measurements are shown in Fig. 6d. In these experiments, the robot lift force reduces as the supplied voltage decreases. As illustrated in Fig. 6d, the reduction of driving voltage V<sub>DEA</sub> causes the balance beam to rotate back to the starting position. To increase the liftoff duration, we can increase the amount of net energy in the storage capacitor C<sub>1</sub>. Fig. 6e-f show the charging and discharging voltage profiles as the storage capacitance increases.

In summary, the static flapping and liftoff experiments demonstrated the ICP-TENG can generate high voltage signals for powering the DEA-driven MAVs. The MAVs can achieve a maximum lift-to-weight ratio of 1.75, which is sufficient for carrying small payloads such as gyroscope[36], magnetometer[37], and camera[38]. However, the ICP-TENG cannot operate the MAVs in real time because the output power cannot satisfy a DEA's high power requirement. To resolve this challenge, we designed energy storage and control circuits that gradually store the energy and impulsively release it onto the DEA. In the next section, we will describe the advantages and limitations of this design. We will further discuss future directions for TENG-based soft robotic driver systems.

### 3. Conclusion

In this work, we proposed an ICP-TENG design that combines the main TENG and secondary charge pumps in the same plane for powering high-voltage and high-power MAVs. This compact design is suitable for mobile robotic systems that have difficulty carrying separate charge pumps due to constrained payload and space. Compared to conventional free-standing mode TENGs, our ICP-TENG shows 280% and 920% increase of output voltage and energy. This substantial improvement enables the first liftoff demonstration

performed by a TENG-powered soft aerial robot. With rectifying, storage, and control circuit elements, the ICP-TENG driver system generates a 1540 V and 400 Hz signal for powering the robot. The 160 mg robot flaps its wings at 400 Hz with a stroke amplitude of 48°, and it achieves an ascending speed of 29 cm/s. This demonstration corresponds to a lift-to-weight ratio of 1.75, implying that additional sensors could be carried in the future.

In many prior works, TENGs were used to harvest energy and then power sensor networks. This work shows TENGs can also drive high voltage and power dense actuators, and it can enable energetically expensive locomotion such as flight. This result represents an exciting research direction for future development and application of TENGs. Furthermore, we demonstrate soft artificial muscles are advantageous owing to their robustness in dynamic conditions. While rigid microscale actuators such as piezoelectric bimorphs require sinusoidal driving waveforms to avoid fracturing, DEAs can safely operate under square wave driving signals due to material compliance. This property, along with their requirement on high voltage driving signals, makes TENGs particularly suitable for driving DEA-actuated robotic systems. We expect future studies will develop DEA-driven terrestrial, aquatic, and aerial robots that are powered by TENGs.

Our ICP-TENG cannot power flight continuously due to its limited output power density. In this work, the ICP-TENG charges a 4.5 µF capacitor to 1540 V in 420 seconds, which is equivalent to having 13 mW output power. With the voltage doubler and the control circuit, the ICP-TENG can drive the DEA at 2 Hz continuously. While this low frequency actuation is adequate for terrestrial and aquatic locomotion, it is far from achieving continuous flight. There are three directions that future works can focus on. First, the energy storage and control circuits can be improved to enable energy recycling. In the current design, energy is dissipated through a resistor R<sub>2</sub> during the discharge phase, leading to an average power consumption of 1 W. In a prior work[35], we demonstrated a similar robot only consumes 100 mW of power when it is driven

by a commercial amplifier (Trek 2220). The drive electronics will become substantially more efficient if energy can be recycled back to the storage capacitor. Second, our robot aerodynamic efficiency can be improved through varying wing size and flapping frequency. This robot has a high agility[8] when it operates at 400 Hz, but its aerodynamic efficiency is approximately 10 times lower than the state-of-the-art MAVs[39]. To improve the robot's lift to power ratio, future works can scale up the wing size and reduce the flapping-wing frequency. Finally, future studies can continue to improve TENG's net output power through stacking more TENG layers, developing new triboelectric materials, and proposing new geometric designs. We envision future TENGs will power diverse sensors, actuators, and robotic systems in challenging environments.

## 4. Experimental section

## 4.1. Fabrication of ICP-TENG

We prepared the following list of thin film materials for constructing the ICP-TENG: Perfluoroalkoxy alkane (PFA; BB3010-2-12, Scientific Commodities), fluorinated Ethylene Propylene (FEP; BB3090-2-A, Scientific Commodities), Polytetrafluoroethylene (PTFE; 15-2F-12, CS Hyde), polyimide (PI; 18-1F-12, Cole-Parmer), polyetheretherketone (PEEK; 37-2F-26, CS Hyde), polyethylene terephthalate (PET; 48-2F-OC, CS Hyde), polyamide (PA; WL6400, CSTsales.com), and aluminum (Al; WOD AFTR36, WOD Tape). The film thickness of these materials is 50 μm. We also prepared spray glue (Loctite 2267077) and rubber tape (Dualplex) for bonding the different material layers.

First, each film was cleaned with ethyl alcohol and deionized water. Then the film was dried with nitrogen gas. Next, the non-conductive thin films were cut with a CO<sub>2</sub> laser (Versa VLS 3.50). The aluminum film and the rubber tape were cut with an ultraviolet (UV) laser (LPKF U4).

The stator and the rotor were constructed separately. To construct the stator, the aluminum film was spray boned (Loctite 2267077) to a 2 mm acrylic substrate (Jetec). Next, a PFA film was placed on top of the Al<sub>1</sub> electrode, which corresponds to the PFA<sub>1</sub> layer in Fig. 2a. A patterned PA film was placed on the area that was uncovered with PFA<sub>1</sub>. To finish the stator construction, a ring shaped Al<sub>2</sub> electrode was put on the perimeter of the stator so all Al<sub>2</sub> sections were electrically connected during device rotation.

Next, we used the same method for constructing the rotor. The aluminum film was used as the rotor electrode (Al<sub>2</sub> region Fig. 2a), and its configuration prevents wires from entangling during rotation. The rotor electrode was affixed to an acrylic substrate via rubber tape (Dualplex). A charge-pumping layer (PFA<sub>2</sub>) was placed on the area that was uncovered by the Al<sub>2</sub> layer. For experiments shown in Fig. 3b-c, we changed the thin film materials accordingly while maintaining the same design geometry. Unless otherwise indicated, TENGs consist of 4 segments with a diameter of 22.8 cm and are driven at the same rotational speed of 10 rps.

### 4.2. Fabrication of the soft MAV

The robot design and fabrication are based on methods described in a prior work[6]. The robot consists of a carbon fiber airframe, a DEA, a pair of connectors, wings, transmissions, and wing hinges. Fig. S6 (Supplementary Material) describes the DEA fabrication process. First, Elastosil P7670 was mixed at 2000 rpm (Thinky AR-100) and poured on an acrylic substrate. The substrate was spun at 1500 rpm in a spin coater (Specialty Coating Systems, G3P-8). Next, the elastomer layer is thermally cured at 60°C for 5 minutes. A mask was placed on top of the cured elastomer layer, and then single-walled carbon nanotube (SWCNT) was transferred onto the elastomer as electrode. This process was repeated 6 times to construct a multi-layered structure. Next, a programmable cutter (Silhouette Cameo) traced a 52 mm x 9 mm

rectangle to release the elastomer multilayer. The electrode layers (blue and red colored contours in Fig. S6, Supplementary Material) were offset by 0.5 mm for making wire connections. This elastomer-electrode multilayer was rolled manually into a cylindrical shell, and then conductive carbon fiber plates were placed on its two ends. After the DEA was constructed, electrical wires were connected to both plates.

The robot airframe, wings, transmissions, wing hinges, and connectors were made by the smart composite manufacturing (SCM) method[40]. The airframe consisted of 8 planar carbon fiber components, and it was manually assembled. The connectors consisted of a fiber glass plate and a carbon fiber plate. The wings were made of polyester thin film, adhesive, and carbon fiber. The wing hinges and transmissions consisted of carbon fiber, polyimide, and adhesive. The polyimide material served as compliant flexures in these structures. In the assembly process, the transmissions were first installed on the airframe. Next, the connectors were affixed to the transmission. Following this step, the DEA is assembled into the airframe. Finally, a pair of robot wings and hinges were inserted into the robot transmissions. The assembled robot is illustrated in Fig. S6 (Supplementary Material).

### 4.3. ICP-TENG characterization experiments

The following components were used to construct the circuit in Fig. 5: silver-coated copper wire (EPX343HT, SME), capacitors (399-19719-ND, 399-13875-ND, KEMET), diodes (2721-DD1000TR-ND, Diotec Semiconductor), high-voltage N-Channel MOSFETs (G3R450MT17D, GeneSiC Semiconductor), and zener diodes (1N5281B, Microchip Technology). An oscilloscope (TDS2000, Tektronix) equipped with a high voltage probe (P5100A, Tektronix) was used to measure the ICP-TENG's output voltage. To precisely control the TENG rotational speed during characterization experiments, a motor (BL34E27, Lin

Engineering) was set up to drive the ICP-TENG. The motor rotational speed varied from 2 to 20 rps in different experiments.

## **CRediT** authorship contribution statement

Y.L. and Y.C. conceived the idea, designed the experiments, and fabricated the TENG. S.K., Y.-H.H., Y.L., and Y.C. fabricated the soft flies. Y.L., Z.R., and Y.-H.H. conducted the experiments. Y.L., Z.R., W.J.S., Y.-H.H., and Y.C. analyzed the data. Y.L. and Y.C. wrote the manuscript. All authors discussed the results and commented on the manuscript.

# **Declaration of Competing Interest**

The authors declare that they have no known competing financial interests or personal relationships that could have appeared to influence the work reported in this paper.

# Acknowledgements

This work was supported by the National Research Foundation of Korea (NRF) (No. 2021R1C1C2009703). It is also supported by the National Science Foundation (FRR-2202477 and FRR-2236708). Any opinions, findings, and conclusions or recommendations expressed in this material are those of the authors and do not necessarily reflect the views of the National Science Foundation. Yi-Hsuan Hsiao is supported by the MathWorks Engineering Fellowship.

# Data availability

Data will be made available on request.

#### References

- [1] R.J. Wood, E. Steltz, R. Fearing, Sensors and Actuators A: Physical, 119 (2005) 476-488.
- [2] D.S. Drew, N.O. Lambert, C.B. Schindler, K.S. Pister, IEEE Robotics and Automation Letters, 3 (2018) 2807-2813.
- [3] K.Y. Ma, P. Chirarattananon, S.B. Fuller, R.J. Wood, Science, 340 (2013) 603-607.
- [4] M.A. Graule, P. Chirarattananon, S.B. Fuller, N.T. Jafferis, K.Y. Ma, M. Spenko, R. Kornbluh, R.J. Wood, Science, 352 (2016) 978-982.
- [5] Y. Chen, E.F. Helbling, N. Gravish, K. Ma, R.J. Wood, 2015 IEEE/RSJ International Conference on Intelligent Robots and Systems (IROS), IEEE2015, pp. 331-338.
- [6] Y. Chen, H. Zhao, J. Mao, P. Chirarattananon, E.F. Helbling, N.-s.P. Hyun, D.R. Clarke, R.J. Wood, Nature, 575 (2019) 324-329.
- [7] T. Bu, T. Xiao, Z. Yang, G. Liu, X. Fu, J. Nie, T. Guo, Y. Pang, J. Zhao, F. Xi, Advanced Materials, 30 (2018) 1800066.
- [8] Y. Chen, S. Xu, Z. Ren, P. Chirarattananon, IEEE Transactions on Robotics, 37 (2021) 1752-1764.
- [9] X. Ji, X. Liu, V. Cacucciolo, M. Imboden, Y. Civet, A. El Haitami, S. Cantin, Y. Perriard, H. Shea, Science Robotics, 4 (2019) eaaz6451.
- [10] Z. Ren, J. Yang, S. Kim, Y.-H. Hsiao, J. Lang, Y. Chen, 2023 IEEE International Conference on Robotics and Automation (ICRA), IEEE2023, pp. 3397-3403.
- [11] F.-R. Fan, Z.-Q. Tian, Z.L. Wang, Nano energy, 1 (2012) 328-334.

- [12] T. Zhou, C. Zhang, C.B. Han, F.R. Fan, W. Tang, Z.L. Wang, ACS applied materials & interfaces, 6 (2014) 14695-14701.
- [13] X. Liang, T. Jiang, G. Liu, T. Xiao, L. Xu, W. Li, F. Xi, C. Zhang, Z.L. Wang, Advanced Functional Materials, 29 (2019) 1807241.
- [14] R. Lei, Y. Shi, Y. Ding, J. Nie, S. Li, F. Wang, H. Zhai, X. Chen, Z.L. Wang, Energy & Environmental Science, 13 (2020) 2178-2190.
- [15] W. Tang, T. Jiang, F.R. Fan, A.F. Yu, C. Zhang, X. Cao, Z.L. Wang, Advanced Functional Materials, 25 (2015) 3718-3725.
- [16] L. Xu, T.Z. Bu, X.D. Yang, C. Zhang, Z.L. Wang, Nano Energy, 49 (2018) 625-633.
- [17] Y. Lee, S.H. Cha, Y.-W. Kim, D. Choi, J.-Y. Sun, Nature Communications, 9 (2018) 1804.
- [18] Y. Lee, S. Lim, W.J. Song, S. Lee, S.J. Yoon, J.M. Park, M.G. Lee, Y.L. Park, J.Y. Sun, Advanced Materials, 34 (2022) 2108586.
- [19] W.J. Song, Y. Lee, Y. Jung, Y.-W. Kang, J. Kim, J.-M. Park, Y.-L. Park, H.-Y. Kim, J.-Y. Sun, Science Advances, 7 (2021) eabg9203.
- [20] Z. Wen, M.-H. Yeh, H. Guo, J. Wang, Y. Zi, W. Xu, J. Deng, L. Zhu, X. Wang, C. Hu, Science Advances, 2 (2016) e1600097.
- [21] X. Chen, T. Jiang, Z.L. Wang, Applied Physics Letters, 110 (2017).
- [22] S. Roy Barman, Y.-J. Lin, K.-M. Lee, A. Pal, N. Tiwari, S. Lee, Z.-H. Lin, ACS Nano, 17 (2023) 2689-2701.
- [23] S.R. Barman, S.-W. Chan, F.-C. Kao, H.-Y. Ho, I. Khan, A. Pal, C.-C. Huang, Z.-H. Lin, Science Advances, 9 (2023) eadc8758.
- [24] S.-H. Jeong, Y. Lee, M.-G. Lee, W.J. Song, J.-U. Park, J.-Y. Sun, Nano Energy, 79 (2021) 105463.
- [25] Y. Yang, H. Zhang, Z.-H. Lin, Y.S. Zhou, Q. Jing, Y. Su, J. Yang, J. Chen, C. Hu, Z.L. Wang, ACS Nano, 7 (2013) 9213-9222.
- [26] W. Liu, Z. Wang, C. Hu, Materials Today, 45 (2021) 93-119.
- [27] J.H. Lee, R. Hinchet, S.K. Kim, S. Kim, S.-W. Kim, Energy & Environmental Science, 8 (2015) 3605-3613.
- [28] Y. Lee, W. Kim, D. Bhatia, H.J. Hwang, S. Lee, D. Choi, Nano Energy, 38 (2017) 326-334.
- [29] W. Xu, H. Zheng, Y. Liu, X. Zhou, C. Zhang, Y. Song, X. Deng, M. Leung, Z. Yang, R.X. Xu, Nature, 578 (2020) 392-396.
- [30] H. Wu, N. Mendel, S. van Der Ham, L. Shui, G. Zhou, F. Mugele, Advanced M aterials, 32 (2020) 2001699.
- [31] Y. Bai, L. Xu, S. Lin, J. Luo, H. Qin, K. Han, Z.L. Wang, Advanced Energy Materials, 10 (2020) 2000605.
- [32] H. Guo, X. Pu, J. Chen, Y. Meng, M.-H. Yeh, G. Liu, Q. Tang, B. Chen, D. Liu, S. Qi, Science Robotics, 3 (2018) eaat2516.
- [33] W. Liu, Z. Wang, G. Wang, G. Liu, J. Chen, X. Pu, Y. Xi, X. Wang, H. Guo, C. Hu, Nature Communications, 10 (2019) 1426.
- [34] D. Choi, Y. Lee, Z.-H. Lin, S. Cho, M. Kim, C.K. Ao, S. Soh, C. Sohn, C.K. Jeong, J. Lee, ACS Nano, (2023).
- [35] Z. Ren, S. Kim, X. Ji, W. Zhu, F. Niroui, J. Kong, Y. Chen, Advanced Materials, 34 (2022) 2106757.
- [36] S.B. Fuller, E.F. Helbling, P. Chirarattananon, R.J. Wood, IMAV 2014: International Micro Air Vehicle Conference and Competition 2014, Delft, The Netherlands, August 12-15, 2014, Delft University of Technology2014.
- [37] E.F. Helbling, S.B. Fuller, R.J. Wood, 2014 IEEE international Conference on Robotics and Automation (ICRA), IEEE2014, pp. 5516-5522.
- [38] S. Mange, E.F. Helbling, N. Gravish, R.J. Wood, 2017 IEEE International Conference on Robotics and Automation (ICRA), IEEE2017, pp. 5409-5414.
- [39] N.T. Jafferis, E.F. Helbling, M. Karpelson, R.J. Wood, Nature, 570 (2019) 491-495.
- [40] J.P. Whitney, P.S. Sreetharan, K.Y. Ma, R.J. Wood, Journal of Micromechanics and Microengineering, 21 (2011) 115021.